

Polarization-controlled non-Hermitian metasurfaces for ultra-sensitive terahertz sensing

Xintong Shi¹, Hai Lin^{1,*}, Tingting Liu^{2,3}, Yun Shen^{4,*}, Rongxin Tang⁴, Le Li⁴, Junyi Zhang^{1,4}, Yanjie Wu⁵, Shouxin Duan⁴, Chenhui Zhao⁴ Shuyuan Xiao^{2,3,*}

1 College of Physics Science and Technology, Central China Normal University, Wuhan 430079, China

2 School of Information Engineering, Nanchang University, Nanchang 330031, China

3 Institute for Advanced Study, Nanchang University, Nanchang 330031, China

4 Institute of Space Science and Technology, Nanchang University, Nanchang 330031, China

5 School of Electronic Science and Engineer, University of Electronics Science and Technology of China, Chengdu 611731, China

*Corresponding author:

linhai@mail.ccnu.edu.cn;

shenyun@ncu.edu.cn;

syxiao@ncu.edu.cn

Abstract

Exceptional points (EPs), where eigenvalues and eigenstates coalesce, offer significant advantages in sensor design. However, the extreme sensitivity near EPs poses significant challenges due to fabrication errors and noises, which degrade sensing performance. To address this, we introduce a novel approach leveraging the polarization degree of freedom to achieve controllable EPs. By expressing tunable polarization as equivalent gain, we establish a direct relation between the polarization of the incident light and the phase of the coupled system, and achieve the polarization-controlled singularity even post-fabrication. The polarization angle can be utilized as a sensing index, which enables indirect and accurate measurement near the EPs. The theoretical approach is experimentally validated using a general design of THz non-Hermitian metasurface sensors. Our results indicate that this method enhances robustness and sensitivity, opening new avenues for practical applications in ultra-sensitive sensing.

Keywords: non-Hermitian, Metasurfaces, Exceptional Points, Singularity, Terahertz Sensor

Introduction

The exceptional points (EPs) are exotic degenerate states in non-Hermitian systems, where the eigenvalues and corresponding eigenstates simultaneously coalesce(1–4). They have been observed in various platforms, such as optics, acoustics, microwaves, and electronics(5–10). The intriguing properties of EPs(11–15) have inspired numerous exciting applications, for example, the EP-based topological lasers(16), the unclonable physical keys(17), and the more flexible wavefront manipulation and topological engineering(18, 19). Additionally, leveraging the eigenvalue splitting near the EP can facilitate the design of high-performance sensors in various photonic structures, such as optical resonators, microcavity, and metasurfaces(20–28). Among them, metasurfaces are highly favored due to their unprecedentedly flexible and versatile design strategies(29–34), and in particular provide feasible solutions in previously inaccessible THz regime. Their significantly enhanced local field(35–37), combined with the EPs, have shown tremendous advantages in detecting weak biological fingerprint responses(38–40).

Despite their superior performance, a critical issue has been consistently overlooked in the existing design strategies for EPs-based metasurface sensors. The ultra-sensitivity near the EPs, while offering significant advantages, can also pose substantial challenges for the micro/nanofabrication, making it a double-edged sword(41). The factors causing eigenvalue splitting include not only the perturbation from the analytes but also fabrication errors, which would lead to a significant degradation in sensing performance. Considering the geometric parameters are fixed once the structures are fabricated, some studies have introduced gain media to compensate for fabrication errors(42). However, such approach is not suitable for periodic structures like metasurfaces, let alone the lack of such gain media in the terahertz regime. This issue appears to be a deadlock, severely obstructing the practical application of non-Hermitian metasurface sensors.

In this work, we resort to the polarization degree of freedom to achieve controllable EPs for improving the sensing performance. We introduce a concept of equivalent gain to express the tunable polarization and construct the non-Hermitian Hamiltonian matrix based on the coupled mode theory including both loss and gain. By solving its eigenvalues, we establish the direct relation between the polarization of incident light and the phase of coupled system, and observe a singularity in the polarization space of EPs. Based on this, the polarization angle, which can be easily tuned for phase singularity at EPs even after fabrication, is utilized as the sensing index. Finally, the theoretical method is experimentally demonstrated using a general design of THz non-Hermitian metasurface sensor. The proposed method explores the new degree of freedom in non-Hermitian physics, and open an avenue for robust ultra-sensitive sensing.

Results

Considering a metasurface, as shown in Figure 1a, a unit cell of a coupled system is constructed by two orthogonal resonators with different damping rates. The resonators, denoted as R_1 and R_2 , possess similar frequencies but distinct damping rates, γ_1 and γ_2 , respectively. The coupling strength between the resonators is represented by κ . Upon illumination of the metasurface with linearly polarized light at a polarization angle θ , the polarization can be decomposed into two orthogonal directions aligned with the resonators. Specifically, the x -polarization and y -polarization are denoted as $E_x =$

$E_0 \cos \theta$ and $E_y = E_0 \sin \theta$, respectively. In each direction, the polarization angle determines the strength of excitation. The amplitude of the incident signal is directly proportional to the intensity of excitation on the resonators. It is important to note that the physical dimensions of damping rate and amplitude differ. To address this, we convert the amplitude (V/m) of excitation to gain (Hz), taking into account the resistance (Ohm) to damping rate (Hz) transformation (For further details, refer to the supplementary material S1.) Consequently, the system is described by the coupled mode equation(43):

$$\frac{\partial a_1}{\partial t} = (\omega_1 - i\gamma_1 + iG_1)a_1 + \kappa a_2, \quad (1)$$

$$\frac{\partial a_2}{\partial t} = (\omega_2 - i\gamma_2 + iG_2)a_2 + \kappa a_1, \quad (2)$$

here, G_1 and G_2 represent the gains on the two resonators corresponding to E_x and E_y , respectively. The coupled mode equation can be reformulated in the Hamiltonian matrix form as follows,

$$H = \begin{bmatrix} \omega_1 - i\gamma_1 + iG_1 & \kappa \\ \kappa & \omega_2 - i\gamma_2 + iG_2 \end{bmatrix}, \quad (3)$$

The corresponding eigenvalues are:

$$\lambda_{\pm} = \Sigma\omega/2 \pm \sqrt{\Delta\omega^2 - 4\kappa^2}/2, \quad (4)$$

here, $\Delta\omega = \omega_1 - \omega_2 + i(G_1 - \gamma_1 - G_2 + \gamma_2)$, and $\Sigma\omega = \omega_1 + \omega_2 + i(G_1 - \gamma_1 + G_2 - \gamma_2)$. The two eigenvalues coalescing at EP means the equation satisfying with the discriminant of a quadratic equation $\Delta\omega^2 - 4\kappa^2 = 0$. At the point, the eigenvalues both are $\lambda_{EP} = \Sigma\omega/2$, and the corresponding expression of phase is:

$$\varphi_{EP} = \arg(\lambda_{EP}) = \arctan \frac{G_1 - \gamma_1 + G_2 - \gamma_2}{\omega_1 + \omega_2} \pm n\pi, (n = 0, 1, -1). \quad (5)$$

We focus on the first quadrant of the function to consider the partition function of $\arg(\lambda_{EP})$. Within a small range, given that $\gamma_i + G_i \ll \omega_i$ (where $i = 1, 2$), we assume $\kappa \approx \Delta\omega/2$. Therefore, we can utilize $\varphi_{EP} = \arg(\lambda_{EP})$ to approximately determine the relation between the polarization angle and frequency near the EP. By employing the arctangent function graph, the undefined point should satisfy $\omega_1 = \omega_2 = 0$. By varying the polarization angle, the sign of $G_1 - \gamma_1 + G_2 - \gamma_2$ will shift, resulting in a 2π transition in $\arg(\lambda_{EP})$. At the singularity point, the group delay becomes infinite and changes from positive to negative. The location of the singularity is determined by the damping rates of the resonators. It is essential that the effective gain $G_1 + G_2$ is greater than the damping rates $\gamma_1 + \gamma_2$; otherwise, the singularity will not manifest.

Figure 1b illustrates the calculated phase distribution, represented by color, within the frequency range of -0.1 to 0.1 Hz and the angle range of 0 to 90 degrees. The description shows a relation between the damping rates and effective gain in the calculation. By observing along the y-axis, the phase distribution exhibits variation with frequency, either leading or lagging. This behavior aligns with the phase transformation near resonance. The phase transitions from a lagging to a leading state, around the distinct boundary. From the phase expression, it is evident that the boundary occurs at $G_1 + G_2 = \gamma_1 + \gamma_2$. In the given parameter configuration, the singularity emerges at 40.95 degree. Importantly, it is notable that there exists only one phase singularity in this quadrant. To provide a clearer understanding of the behavior, three

lines corresponding to 30, 40, and 50 degrees are extracted from the figure and plotted as phase-frequency curves, illustrated by white dotted lines in Figure 1c. The phase exhibits a distinct transformation on both sides of the singularity point. As closer to this point, the phase reversal occurs at a faster rate. It is important to note that the phase singularity is influenced by the polarization, thus establishing a polarization-controlled singularity system.

However, it is important to acknowledge that in reality, the frequency cannot be zero. Therefore, in the aforementioned equations, ω_1 and ω_2 should represent the difference between the eigenfrequency and the excitation frequency. Consequently, the condition for singularity in an actual system is $\omega_1 - \omega = 0$ and $\omega_2 - \omega = 0$, indicating that the eigenfrequencies of the resonators match the excitation frequency.

Subsequently, we can establish the sensing function with respect to the polarization angle. Based on the discriminant of the eigenvalue, $\Delta\omega^2 - 4\kappa^2 = 0$, the system satisfies the following conditions,

$$2\kappa = \omega_1 - \omega_2 + i(G_1 - \gamma_1 - G_2 + \gamma_2). \quad (6)$$

When an analyte is introduced onto the metasurface, it perturbs the system, causing the eigenfrequencies to become $\omega_i - \Delta\omega_i - i\gamma_i - i\Delta\gamma_i$, (where $i = 1, 2$), and the eigenvalues will split. The magnitude of the split is denoted as $\delta = \sqrt{(\Delta\Omega + i(\Delta\Gamma))^2 - 4\kappa^2}$, where, $\Delta\Omega = \omega_1 - \Delta\omega_1 - (\omega_2 - \Delta\omega_2) = \Delta\omega_2 - \Delta\omega_1$, $\Delta\Gamma = G_1 - G_2 - \gamma_1 + \gamma_2 - \Delta\gamma$. The plot of δ exhibits a self-crossing Riemann surface, as depicted in Figure 1c. This form of the eigenvalue represents an important characteristic of a non-Hermitian system. The EP occurs at the point where the real part and imaginary part coalesce simultaneously.

Introducing a perturbation in the system results in the splitting of the real part of δ , while the imaginary part still exhibits a zero-crossing line. When the imaginary part equals zero, the phase of the system can be expressed as:

$$\varphi_{\pm} = \arctan \frac{\bar{\Gamma}}{\pm\sqrt{\Delta\Omega^2 - \Delta\Gamma^2 - 4\kappa'^2 + 4\kappa''^2}}, \quad (7)$$

here, $\bar{\Gamma} = G_1 + G_2 - \gamma_1 - \gamma_2 - \Delta\gamma$, $\Delta\Gamma = G_1 - G_2 - \gamma_1 + \gamma_2 - \Delta\gamma$, κ' and κ'' represent the real and imaginary parts of the coupling strength, respectively (For more details on the coupling strength, please refer to Supplementary S2). The phase singularity occurs when the denominator approaches zero. To facilitate the identification of the singularity, we differentiate the phase with respect to frequency. The maximum or minimum of the group delay corresponds to the singularity. This operation and setting $\omega_1 = \omega_2 = 0$ are diverse but congruent.

Considering that the numerator of the phase expression is $\bar{\Gamma}$, we can derive the relation between the polarization angle and the singularity of the group delay,

$$D = \frac{\sin\theta + \cos\theta - \gamma_0}{-2\gamma_0(\sin\theta + \cos\theta) + \sin 2\theta - 2\omega_0\omega + \gamma_0^2 + \omega_0^2 + \omega^2 + 1}, \quad (8)$$

here, D represents the group delay, γ_0 is original parameter of the unload sensor. Figure 1d illustrates the relation between the group delay and the polarization angle with $\bar{\Gamma} = 0.1$. As the polarization angle changes, the group delay undergoes a transition near a singular point, shifting from positive to negative. This point represents a unique undefined value on the polarization axis. This relation establishes the polarization angle as an indicator for the state of the sensor.

Currently, the majority of studies on non-Hermitian sensing primarily focus on the frequency splitting observed in the spectrum, which can be viewed as a projection of EPs in the amplitude-frequency domain. By utilizing the phase-frequency domain to explore EP singularities, we can observe another projection, namely the phase singularity. In a similar vein, Equation 8 serves as a method to observe the singularity of EPs that we have developed. We propose a step-by-step procedure for implementing this method in sensing applications.

Initially, the constant parameter in Equation 8 can be determined by switching the polarization and measuring the corresponding responses without loading any analyte. Subsequently, when a perturbation is introduced into the system, the new polarization associated with the singularity can be determined. Employing this method helps to avoid unstable(41) measurements at the singularity, thereby improving measurement accuracy. Furthermore, compared to direct measurements, responses obtained from locations far away from the singularity exhibit greater stability and are less susceptible to interference. This leads to more accurate results and allows for solution derivation based on a set of measurement data, thereby reducing the impact of measurement errors on the final outcomes.

To validate this method, we employ the finite integration technique to design a metasurface sensor, which consists of simple and classical structures, namely split ring resonators (SRRs) and cut wires. The selection of these simple structures ensures manageable responses while maintaining sufficient coupling effects. The initial parameters of the structures, including the SRRs and cut wires, are estimated using the ruler equation(44). Subsequently, the parameters are adjusted to align the resonances to the same frequency. By combining these two structures into a single unit, a coupled system was formed. Figure 2a provides a schematic illustration of the metasurface configuration. We conduct simulations to obtain the phase response of the metasurface without any analytes under different polarizations. The designed parameters of the metasurface sensor are presented in Table 1, and the corresponding results are plotted in Figure 2b.

The range of frequency from 0.82 to 0.84 THz, the range of polarization angle from 0 to 90 degrees. The singularity appears at 42 degree and 0.827 THz. Closer to the singularity point, the phase variation becomes more pronounced. It is easy to observe that the simulation result agrees with the theoretical calculations.

In the numerical simulation, a 20 μm dielectric layer is introduced onto the metasurface sensor to simulate the analyte(45). The refractive index range considered is from 1 to 1.2, while the polarization angle is varied between 40 and 50 degrees. The simulation results are presented in Figure 2c, where each pixel represents a simulated response. The horizontal axis represents the polarization angle, while the vertical axis represents the refractive index of the dielectric layer. The color scale indicates the extreme values (maximum or minimum) of the group delay. Notably, a distinct transition is observed, indicating a relation between the two variables characterized by a series of singularities.

Beside the transition region, the group delay exhibits different symbols, with one side being positive and the other side being negative. This transition signifies that within the given range, each value of the refractive index corresponds to a unique polarization angle. Thus, the result demonstrates the existence of a specific correlation between the refractive index and the polarization angle within a defined range.

To illustrate this relation clearly, three specific refractive index parameters (1.05, 1.1, and 1.15) are selected from Figure 2c. Figure 2d depicts the corresponding group delay

values for these refractive indexes. The behavior of the three lines aligns with the theoretical results. Notably, at polarization angles of 43° , 45° , and 46° , the group delays undergo a transition from positive to negative, revealing the presence of phase singularities. In essence, these findings demonstrate that the polarization angles can effectively determine the refractive index.

However, it is important to note that the refractive index of analytes in different concentrations is not the only factor affecting terahertz biosensing. The effective refractive index varies depending on the properties of the substrate and the attached material. Additionally, terahertz detection often involves the removal of moisture, further complicating the use of refractive index alone for accurate terahertz biosensing. To address this, it is necessary to simulate different concentrations of analytes by employing dielectric blocks with varying thickness.

Here, we simulate the metasurfaces coated with a dielectric layer of constant refractive index, with the thickness ranging from 0 to $20\ \mu\text{m}$. Two types of dielectric layers with distinct refractive indexes are used to emulate different analytes. The corresponding results are presented in Figure 2e and Figure 2f, revealing that the sensitivity to the thickness parameter is non-linear. While the thickness variation of the dielectric layer is linear, the corresponding polarization angle exhibits a non-linear response. Moreover, as the dielectric layer becomes thicker, the polarization angle undergoes slower changes. Additionally, the polarization angle varies differently depending on the type of dielectric layer, demonstrating the sensor's capability to specifically distinguish between different analytes. Furthermore, the system's response is more sensitive when a thinner dielectric layer is employed, and the curves corresponding to different refractive indexes (representing different analytes) exhibit distinct patterns. Based on this principle, we attribute the sensor with the capability to accurately identify different analytes.

Finally, we also conduct experimental demonstration of the metasurface sensors to validate the proposed method. The analyte used in the experiments is bovine serum albumin (BSA) with varying concentrations. During the measurement process, a switchable linearly polarized terahertz wave is illuminated onto the metasurface sensor at a specific polarization angle θ . The polarization angle of the emitter is precisely controlled by a rotating polarizer. The transmitted signal is then separated into the horizontal axis using a polarizer and subsequently detected by a receiver.

Figure 3a provides an artistic illustration depicting the entire process based on the terahertz time-domain spectrometer, while Figure 3b presents a photograph of the fabricated sensor. To enhance measurement precision, we implement two key measures. Firstly, to minimize the need for frequent adjustments of the polarizer angle, multiple metasurfaces are fabricated, each coated and dried with BSA at different concentrations. Secondly, considering that simultaneously testing two orthogonal polarizations would introduce unnecessary errors due to polarizer changes, potentially affecting the overall measurement system's stability, we omit the singularity in the orthogonal direction during the measurement design. These processes play a crucial role in improving the measurement accuracy.

The calibration procedure involved setting the first polarizer to have the same polarization as the photoconductor antenna, while the polarization of the second polarizer is adjusted to be orthogonal to the first. The second polarizer is carefully aligned to achieve calibration when the transmission amplitude reaches its minimum. The angle of the first polarizer is then set by selecting points at 5-degree intervals

around 45 degrees. After each setting, the unload sensor and other sensors with varying BSA concentrations are sequentially placed on the light path, and a set of responses is measured.

Figures 3c-3f illustrate magnified photographs of the metasurface sensors coated with different concentrations of BSA (0.001, 0.01, 0.1, and 1 $\mu\text{mol/L}$, respectively). In these images, the gray region represents the silicon substrate, the white region corresponds to the aluminum structure, and the black dots represent the analytes.

The processed group delay as shown in figure 3g, the same method depicts the group delay between polarization and concentration. The results have verified the relation between polarization angle and concentration of BSA, it is as similar as the anticipation of theoretical and simulation results. The phase transition of the unload sensor is observed between 40 and 45 degrees. For sensors with concentrations of about 0.001 $\mu\text{mol/L}$, 0.01 $\mu\text{mol/L}$, and 0.1 $\mu\text{mol/L}$, the phase transitions appear between 45 and 50 degrees. Sensors with a concentration of 1 $\mu\text{mol/L}$ of BAS exhibit a transition between 50 and 55 degrees. Based on the proposed theory, we can solve the singularity of each concentration. Then, using the Equation 8, the entire group delay with the polarization from 40 to 60 degrees are depicted in figure 3g. It is clearly that each concentration of BSA matches one polarization singularity. The result corroborates the theory, the singularity on the curve is clear. This method mainly adds precision of measurement for polarization singularity.

Table 2 shows the concentration of BSA, corresponding polarization angle and sensitivity. Referring the define of sensitivity of traditional metasurface sensors(45–50), we use the quotient of degree divided by concentration to express the sensitivity. Due to the instinct characteristic method, but we are not able to take comparison of sensitivity with traditional methods directly. But just based on the results in table 2, the sensor shows more higher sensitivity for low concentration of BSA. Thus, this method is very sensitive for trance analyses. Currently, the measurement is also limited by the spectrometer, which is a challenging. However, we believe that with breakthroughs in technologies, the advantages of this method will surpass other sensors.

Discussion

In summary, we have proposed a novel THz sensing method based on polarization-control singularity to address the current challenges in non-Hermitian metasurface sensors. Starting from a coupled model, we construct a second-order non-Hermitian system using a metasurface platform. By introducing the concept of equivalent gain, we link the polarization of the incident light to the phase singularities achieving polarization tunability at the EPs in a passive non-Hermitian metasurface. Furthermore, we derive a sensor characterization method based on the phase expression of the system's eigenvalues, using the polarization rotation angle as an indicator. We also formulated an equation to locate phase singularities, which circumvents some issues related to directly measuring the response near the EPs, significantly enhancing the sensing performance. It is noted that the performance can be further improved by incorporating sophisticated designs, nonlinear effects, and higher-order coupling. We aspire for this sensing method to augment the application potential of non-Hermitian THz metasurface sensors, and in particular, enhance the stability of non-Hermitian sensor measurements.

References

1. Ş. K. Özdemir, S. Rotter, F. Nori, L. Yang, Parity–time symmetry and exceptional points in photonics. *Nat. Mater.* **18**, 783–798 (2019).
2. Y. Ashida, Z. Gong, M. Ueda, Non-Hermitian physics. *Adv. Phys.* **69**, 249–435 (2020).
3. C. Li, R. Yang, X. Huang, Q. Fu, Y. Fan, F. Zhang, Experimental Demonstration of Controllable PT and Anti- PT Coupling in a Non-Hermitian Metamaterial. *Phys. Rev. Lett.* **132**, 156601 (2024).
4. M. De Carlo, (INVITED) Exceptional points of parity-time- and anti-parity-time-symmetric devices for refractive index and absorption-based sensing. *Results Opt.* **2**, 100052 (2021).
5. M. S. Ergoktas, S. Soleymani, N. Kakenov, K. Wang, T. B. Smith, G. Bakan, S. Balci, A. Principi, K. S. Novoselov, S. K. Ozdemir, C. Kocabas, Topological engineering of terahertz light using electrically tunable exceptional point singularities. *Science* **376**, 184–188 (2022).
6. T. He, Z. Zhang, J. Zhu, Y. Shi, Z. Li, H. Wei, Z. Wei, Y. Li, Z. Wang, C.-W. Qiu, X. Cheng, Scattering exceptional point in the visible. *Light Sci. Appl.* **12**, 229 (2023).
7. Y. Li, X. Ma, Z. Hatzopoulos, P. Savvidis, S. Schumacher, T. Gao, Switching off microcavity polariton condensate near the exceptional point. arXiv:2101.09478 [Preprint] (2021). <http://arxiv.org/abs/2101.09478>.
8. S. H. Park, S.-G. Lee, S. Baek, T. Ha, S. Lee, B. Min, S. Zhang, M. Lawrence, T.-T. Kim, Observation of an exceptional point in a non-Hermitian metasurface. *Nanophotonics* **9**, 1031–1039 (2020).
9. J. W. Rao, Y. T. Zhao, Y. S. Gui, X. L. Fan, D. S. Xue, C.-M. Hu, Controlling Microwaves in Non-Hermitian Metamaterials. *Phys. Rev. Appl.* **15**, L021003 (2021).
10. S. Baek, S. H. Park, D. Oh, K. Lee, S. Lee, H. Lim, T. Ha, H. S. Park, S. Zhang, L. Yang, B. Min, T.-T. Kim, Non-Hermitian chiral degeneracy of gated graphene metasurfaces. *Light Sci. Appl.* **12**, 87 (2023).
11. W. Song, W. Sun, C. Chen, Q. Song, S. Xiao, S. Zhu, T. Li, Breakup and Recovery of Topological Zero Modes in Finite Non-Hermitian Optical Lattices. *Phys. Rev. Lett.* **123**, 165701 (2019).
12. C. Liang, Y. Tang, A.-N. Xu, Y.-C. Liu, Observation of Exceptional Points in Thermal Atomic Ensembles. *Phys. Rev. Lett.* **130**, 263601 (2023).
13. W. Chen, Ş. Kaya Özdemir, G. Zhao, J. Wiersig, L. Yang, Exceptional points enhance sensing in an optical microcavity. *Nature* **548**, 192–196 (2017).
14. M. De Carlo, F. De Leonardis, R. A. Soref, L. Colatorti, V. M. N. Passaro, Non-Hermitian Sensing in Photonics and Electronics: A Review. *Sensors* **22**, 3977 (2022).
15. R. Colom, E. Mikheeva, K. Achouri, J. Zuniga-Perez, N. Bonod, O. J. F. Martin, S. Burger, P. Genevet, Crossing of the Branch Cut: The Topological Origin of a Universal 2π -Phase Retardation in Non-Hermitian Metasurfaces. *Laser Photonics Rev.* **17**, 2200976 (2023).

16. A. Schumer, Y. G. N. Liu, J. Leshin, L. Ding, Y. Alahmadi, A. U. Hassan, H. Nasari, S. Rotter, D. N. Christodoulides, P. LiKamWa, M. Khajavikhan, Topological modes in a laser cavity through exceptional state transfer. *Science* **375**, 884–888 (2022).
17. M. Yang, Z. Ye, H. Pan, M. Farhat, A. E. Cetin, P.-Y. Chen, Electromagnetically unclonable functions generated by non-Hermitian absorber-emitter. *Sci. Adv.* **9**, eadg7481 (2023).
18. Q. Song, M. Odeh, J. Zúñiga-Pérez, B. Kanté, P. Genevet, Plasmonic topological metasurface by encircling an exceptional point. *Science* **373**, 1133–1137 (2021).
19. Z. Yang, P.-S. Huang, Y.-T. Lin, H. Qin, J. Zúñiga-Pérez, Y. Shi, Z. Wang, X. Cheng, M.-C. Tang, S. Han, B. Kanté, B. Li, P. C. Wu, P. Genevet, Q. Song, Creating pairs of exceptional points for arbitrary polarization control: asymmetric vectorial wavefront modulation. *Nat. Commun.* **15**, 232 (2024).
20. J. Wiersig, Sensors operating at exceptional points: General theory. *Phys. Rev. A* **93**, 033809 (2016).
21. J. Wiersig, Review of exceptional point-based sensors. *Photonics Res.* **8**, 1457 (2020).
22. R. Huang, Ş. K. Özdemir, J. Liao, F. Minganti, L. Kuang, F. Nori, H. Jing, Exceptional Photon Blockade: Engineering Photon Blockade with Chiral Exceptional Points. *Laser Photonics Rev.* **16**, 2100430 (2022).
23. B. Jin, W. Tan, C. Zhang, J. Wu, J. Chen, S. Zhang, P. Wu, High-Performance Terahertz Sensing at Exceptional Points in a Bilayer Structure. *Adv. Theory Simul.* **1**, 1800070 (2018).
24. J.-H. Park, A. Ndao, W. Cai, L. Hsu, A. Kodigala, T. Lepetit, Y.-H. Lo, B. Kanté, Symmetry-breaking-induced plasmonic exceptional points and nanoscale sensing. *Nat. Phys.* **16**, 462–468 (2020).
25. M. Sakhdari, M. Farhat, P.-Y. Chen, PT-symmetric metasurfaces: wave manipulation and sensing using singular points. *New J. Phys.* **19**, 065002 (2017).
26. H. Yuan, W. Zhang, Z. Zhou, W. Wang, N. Pan, Y. Feng, H. Sun, X. Zhang, Non-Hermitian Topoelectrical Circuit Sensor with High Sensitivity. *Adv. Sci.* **10**, 2301128 (2023).
27. J. Xu, S. Ouyang, L. Luo, Y. Shen, L. Zou, Z. Tan, X. Deng, Experiment on parity-time-symmetry phase transition in non-Hermitian metasurfaces. *J. Opt. Soc. Am. B* **39**, 1847 (2022).
28. Y. Li, Z. Deng, C. Qin, S. Wan, B. Lv, C. Guan, J. Yang, S. Zhang, J. Shi, Bifunctional sensing based on an exceptional point with bilayer metasurfaces. *Opt. Express* **31**, 492 (2023).
29. Y. Chen, J. Hu, S. Yin, W. Zhang, W. Huang, Bimodal Absorber Frequencies Shift Induced by the Coupling of Bright and Dark Modes. *Materials* **17**, 3379 (2024).
30. S. Yin, D. Zeng, M. Zhang, X. Shi, Y. Lang, W. Huang, W. Zhang, J. Han, Phase mismatch induced suppression of eigenmode resonance in terahertz metasurfaces. *Opt. Express* **30**, 19176 (2022).

31. W. Huang, S. Yin, W. Zhang, K. Wang, Y. Zhang, J. Han, Robust and broadband integrated terahertz coupler conducted with adiabatic following. *New J. Phys.* **21**, 113004 (2019).
32. W. Huang, S.-T. Cao, X. Qu, W. Zhang, S. Yin, J. Han, Inverse Design of Metamaterial Bound States in the Continuum Device via Coupled Mode Theory. *IEEE Trans. Microw. Theory Tech.* **72**, 1520–1528 (2024).
33. S. Yin, Y. Chen, B. Quan, S. Liu, W. Huang, M. Liu, W. Zhang, J. Han, Coupling-enabled chirality in terahertz metasurfaces. *Nanophotonics* **12**, 1317–1326 (2023).
34. S. Singh, R. J. Davis, D. J. Bisharat, J. Lee, S. M. Kandil, E. Wen, X. Yang, Y. Zhou, P. R. Bandaru, D. F. Sievenpiper, Advances in Metasurfaces: Topology, Chirality, Patterning, and Time Modulation. *IEEE Antennas Propag. Mag.* **64**, 51–62 (2022).
35. S.-F. Shi, B. Zeng, H.-L. Han, X. Hong, H.-Z. Tsai, H. S. Jung, A. Zettl, M. F. Crommie, F. Wang, Optimizing Broadband Terahertz Modulation with Hybrid Graphene/Metasurface Structures. *Nano Lett.* **15**, 372–377 (2015).
36. E. Melik-Gaykazyan, K. Koshelev, J.-H. Choi, S. S. Kruk, A. Bogdanov, H.-G. Park, Y. Kivshar, From Fano to Quasi-BIC Resonances in Individual Dielectric Nanoantennas. *Nano Lett.* **21**, 1765–1771 (2021).
37. Y. Liang, X. Liu, J. Xin, X. Zhang, Y. Wang, Y. Song, Ultra-broadband long-wave infrared metasurface absorber based on Peano fractal curve. *Results Phys.* **33**, 105169 (2022).
38. L. Ho, M. Pepper, P. Taday, Signatures and fingerprints. *Nat. Photonics* **2**, 541–543 (2008).
39. X. Shi, Z. Han, Enhanced terahertz fingerprint detection with ultrahigh sensitivity using the cavity defect modes. *Sci. Rep.* **7**, 13147 (2017).
40. S. H. Lee, Y. K. Lee, S.-H. Lee, J. Kwak, H. S. Song, M. Seo, Detection and discrimination of SARS-CoV-2 spike protein-derived peptides using THz metamaterials. *Biosens. Bioelectron.* **202**, 113981 (2022).
41. R. Duggan, S. A. Mann, A. Alù, Limitations of Sensing at an Exceptional Point. *ACS Photonics* **9**, 1554–1566 (2022).
42. X. Lv, Q. Lin, W. Qiu, H. Guan, H. Lu, Non-Hermitian Optical Tunable System Based on Lithium Niobate Coupling Resonator. *IEEE Photonics J.* **14**, 1–5 (2022).
43. H. A. Haus, W. Huang, Coupled-mode theory. *Proc. IEEE* **79**, 1505–1518 (1991).
44. S. Yin, F. Hu, X. Chen, J. Han, T. Chen, X. Xiong, W. Zhang, Ruler equation for precisely tailoring the resonance frequency of terahertz U-shaped metamaterials. *J. Opt.* **21**, 025101 (2019).
45. J. Zhang, N. Mu, L. Liu, J. Xie, H. Feng, J. Yao, T. Chen, W. Zhu, Highly sensitive detection of malignant glioma cells using metamaterial-inspired THz biosensor based on electromagnetically induced transparency. *Biosens. Bioelectron.* **185**, 113241 (2021).

- 46. A. B. Evlyukhin, S. I. Bozhevolnyi, A. Pors, M. G. Nielsen, I. P. Radko, M. Willatzen, O. Albrektsen, Detuned Electrical Dipoles for Plasmonic Sensing. *Nano Lett.* **10**, 4571–4577 (2010).
- 47. R. Singh, W. Cao, I. Al-Naib, L. Cong, W. Withayachumnankul, W. Zhang, Ultrasensitive terahertz sensing with high- Q Fano resonances in metasurfaces. *Appl. Phys. Lett.* **105**, 171101 (2014).
- 48. Y. Wang, Z. Han, Y. Du, J. Qin, Ultrasensitive terahertz sensing with high- Q toroidal dipole resonance governed by bound states in the continuum in all-dielectric metasurface. *Nanophotonics* **10**, 1295–1307 (2021).
- 49. M. Beruete, I. Jáuregui-López, Terahertz Sensing Based on Metasurfaces. *Adv. Opt. Mater.* **8**, 1900721 (2020).
- 50. R. Sun, W. Li, T. Meng, G. Zhao, Design and optimization of terahertz metamaterial sensor with high sensing performance. *Opt. Commun.* **494**, 127051 (2021).

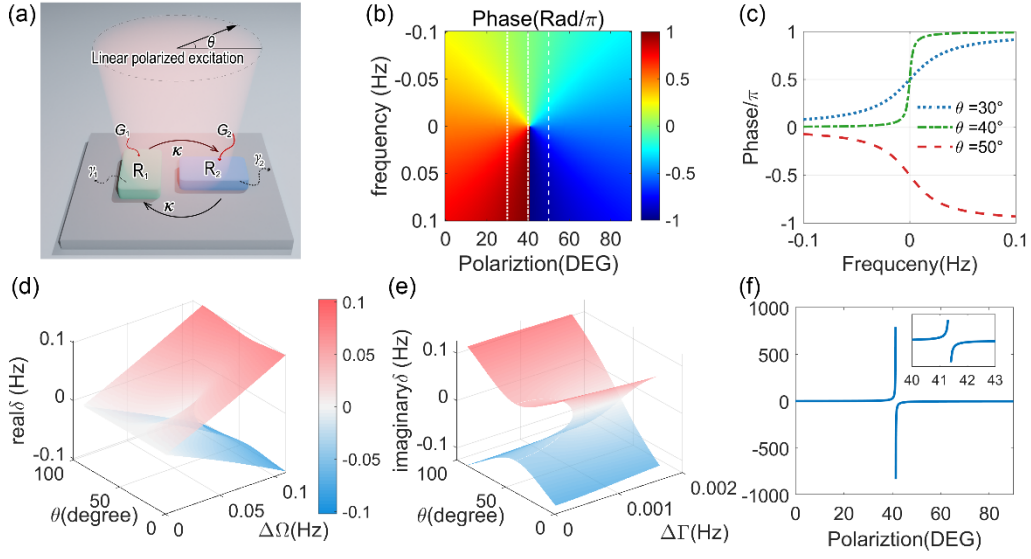


Figure 1 Theoretical predictions. a. The schematic illustration of the metasurface-based coupled system, b. The group delay calculation with respect to the variables frequency and polarization. The parameters used in the calculation are $0.1 < \omega_1 + \omega_2 < 0.1$, $\gamma_1 + \gamma_2 = 0.01$, $G_1 = 0.1 \cos \theta$, and $G_2 = 0.1 \sin \theta$, c. The phase relation at polarizations of 30, 40, and 50 degrees. d, e, and f. The splitting of eigenvalues with the parameters $\Delta\gamma_1 = [0, 0.01]$, $\Delta\gamma_2 = [0, 0.02]$, $\Delta\omega = [0, 0.1]$, $\kappa = 0.03e^{i\pi}$, and $\gamma_1 + \gamma_2 = 0.01$. f. The relation between polarization and group delay. The parameter used in the calculation is $\bar{\Gamma} = 0.1$.

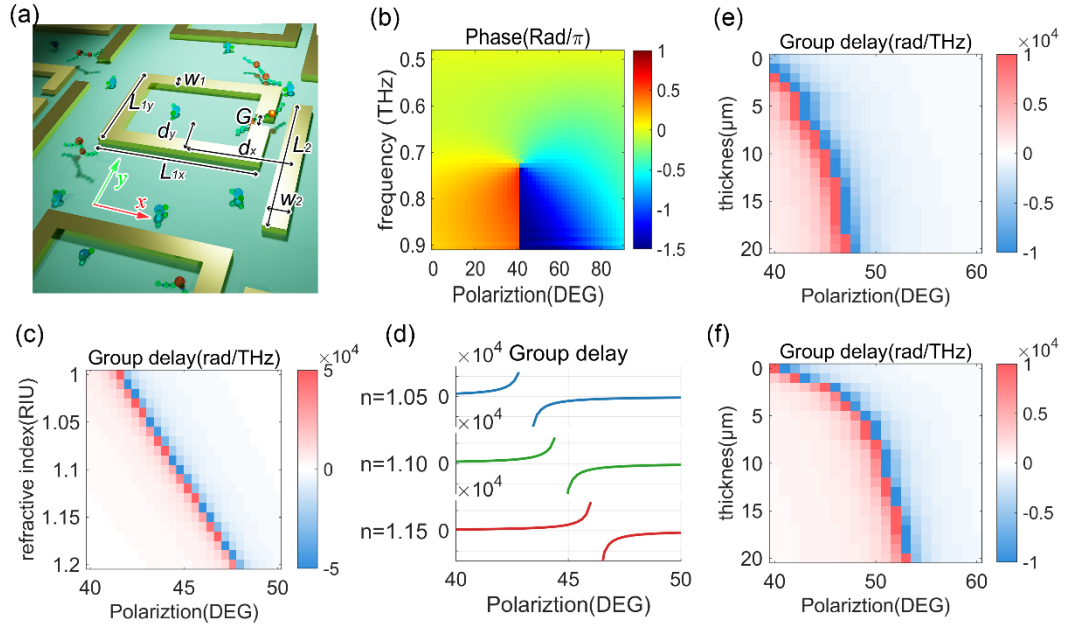


Figure2 Simulation results. a. The schematic of the non-Hermitian THz metasurface sensor. b. The phase distribution without loading analyte, c. The relation between the polarization angle (x -axis) and refractive index (y -axis), with group delay indicated by color. d. The three refractive indexes are extracted from Figure. 2c to illustrate the results. e and f are the group delay with varying the thickness of analytes, with the refractive index are 1.2 and 1.4, respectively.

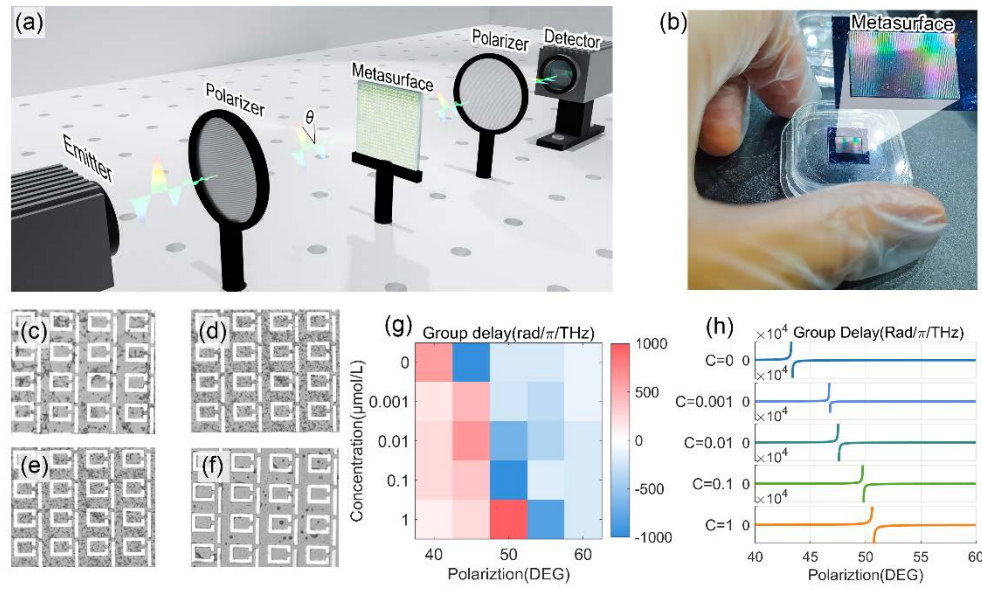


Figure 3. Experiment results. a. The schematic illustration of the measurement system, b. The fabricated sample of metasurface sensor. c-f. The magnified imaging of metasurface sensors coated with BSA of different concentrations, g. The group delay calculated using a set of 5×5 measurements, revealing the relation between polarization angle and concentration. h. The group delay calculated by Equation 8.

Table 1 Parameters of the non-Hermitian THz metasurface sensor

Parameters	Symbols	Values (μm)
Length of SRR in the x direction	L_{lx}	60
Length of SRR in the y direction	L_{ly}	50
Length of wire	L_2	59
Width of SRR	W_1	10
Width of wire	W_2	10
Gap of SRR	G	10
Distance between SRR and wire in the x direction	d_x	42.5
Displacement of SRR from the center of unit cell in the y direction	d_y	20

Table2 The concentration, polarization and sensitivity

Concentration ($\mu\text{mol/L}$)	0	0.001	0.01	0.1	1
Polarization (degree)	43.31	46.72	47.54	49.78	50.67
Sensitivity (degree/ $\mu\text{mol/L}$)	—	3410	423	64.7	7.63